

Customized Luminescent Multiplexed Quick-Response Codes as Reliable Temperature Mobile Optical Sensors for eHealth and Internet of Things

João F. C. B. Ramalho, Lília M. S. Dias, Lianshe Fu, Alexandre M. P. Botas, Luís D. Carlos, Albano N. Carneiro Neto, Paulo S. André,* and Rute A. S. Ferreira*

The need to sense and track in real time through sustainable and multifunctional labels is exacerbated by the COVID-19 pandemic, where the simultaneous measurement of body temperature and the fast tracking of people is required. One of the big challenges is to develop effective low-cost systems that can promote healthcare provision everywhere and for that, smarter and personalized Internet of things (IoT) devices are a pathway in large exploration, toward cost reduction and sustainability. Using the concept of color-multiplexed quick response (QR) codes, customized smart labels formed by two independent layers and smart location patterns provide simultaneous tracking and multiple synchronous temperature reading with maximum sensitivity values of $8.5\% \text{ K}^{-1}$ in the physiological temperature range, overwhelming the state-of-the-art optical sensor for healthcare services provided electronically via the internet (eHealth) and mobile sensors (mHealth).

1. Introduction

Internet of things (IoT) and health are two fields that have the potential to grow together. From their connection arises the concept of eHealth which refers essentially to the use of information and communication technologies in healthcare services.^[1,2] This concept benefits from the advances of intelligent and integrated technological systems that are expected to live in and onto our bodies in different forms of flexible wearables.^[3,4] Healthcare assisted by portable and wireless technologies is often termed mobile health (mHealth),^[5,6] in which smartphones stand out as the most used ones. The combination of eHealth and mHealth enables monitoring and health tracking, providing vital

information for remote medicine analysis (or in point of care) and successfully detecting health abnormalities.^[7] Moreover, eHealth and mHealth can mitigate the lack of infrastructural or human resources in underprivileged regions.^[1]


Requisites for eHealth and mHealth medical devices are being designed for customized in-home care toward continuous and noninvasive monitoring.^[8] Among the vital signals, body temperature stands out as the easiest and typically monitored one by common persons to infer the health condition. The pandemic scenario exacerbated such need for sense in real time through sustainable and multifunctional labels of body temperature and the fast tracking of people information (e.g., COVID-19 test results, places visited).

The near-infrared (NIR) thermal cameras are one of the main devices used due to the fast response times and noninterference to electromagnetic fields in the working environment. Nonetheless, ambient conditions (e.g., stray light, reflected radiation, flame, or gas steam) may lead to temperature uncertainty of up to 1–8%.^[9] In addition, the temperature readout requires human resources, being time-consuming and error prone, and people tracking is not possible to be done simultaneously. The recent reports on mobile optical sensing mediated by smartphones appear as an intriguing strategy to enable large-scale sensing and tracking mediated by the user.^[10] Very few works address simultaneously sensing and tracking,^[10–13] most of the reports focused only on temperature sensing, though photographic records from the luminescent materials recorded with a

J. F. C. B. Ramalho, L. M. S. Dias, A. M. P. Botas, L. D. Carlos, A. N. Carneiro Neto, R. A. S. Ferreira
Department of Physics and CICECO—Aveiro Institute of Materials
University of Aveiro
3810-193 Aveiro, Portugal
E-mail: rferreira@ua.pt

L. Fu
Department of Physics and Department of Chemistry and CICECO - Aveiro
Institute of Materials
University of Aveiro
3810-193 Aveiro, Portugal

P. S. André
Department of Electrical and Computer Engineering and Instituto de
Telecomunicações, Instituto Superior Técnico
Universidade de Lisboa
1049-001 Lisbon, Portugal
E-mail: paulo.andre@lx.it.pt

 The ORCID identification number(s) for the author(s) of this article can be found under <https://doi.org/10.1002/adpr.202100206>.

© 2021 The Authors. Advanced Photonics Research published by Wiley-VCH GmbH. This is an open access article under the terms of the Creative Commons Attribution License, which permits use, distribution and reproduction in any medium, provided the original work is properly cited.

DOI: 10.1002/adpr.202100206

smartphone or a digital camera.^[14–16] The thermometric parameter relies on the color variation arising from intensity variations. This offers consistent measurements and avoids some of the problems identified in other thermometric parameters, such as intensity changes due to inhomogeneities in the concentration of the emitting centers or excitation source power fluctuations.^[17–20] However, some recent works raise concerns on the reliability of the technique caused by experimental artifacts.^[21–28] One solution to overcome these limitations is the use of primary thermometers characterized by a well-established equation (e.g., Varshni's law for semiconductor nanoparticles^[21,29] or Boltzmann distribution when using intensity ratio between two thermally coupled levels^[13,30–35]), where all parameters are known without the need of a prior calibration. Nonetheless, the theoretical knowledge of the mechanism behind the emission dependence on the temperature is unattainable in most cases, disabling the a priori building of a primary thermometer. Moreover, a comprehensive theoretical description of the mechanisms behind luminescence thermometry was only established for single-ion Boltzmann-based systems. New approaches combining experiment and theoretical calculations are, therefore, desirable for other ratiometric luminescent thermometers such as energy-driven ones.^[36]

From the practical temperature-sensing point of view, luminescent quick response (QR) codes stand out as smart labels able to provide sensing and allowing the data to be sent over the IoT network, enabling the tracking functionality.^[10] QR codes act as the gateway to IoT due to the growing use of smartphones/mobile devices and their properties such as fast and easy reading, capacity to store more information than that found in conventional codes, and versatility associated with the rapid and simplified access to information.^[13,37] An intriguing example is the use of colored multiplexed luminescent QR codes based on organic–inorganic hybrids (e.g., diureasils^[38]) modified by trivalent lanthanide (Ln^{3+}) ions. The photograph of the QR code taken with the charged-coupled device (CCD) camera of a smartphone is used to measure the temperature through the intensity ratio between the red (R), green (G), and blue (B) coordinates with maximum relative sensitivity (S_m) and minimum temperature uncertainty (δT_m), at 293 K, of $5.14\% \text{ K}^{-1}$ and 0.194 K , respectively.^[13] Despite this promising result, when thinking about eHealth and mHealth challenges concerning security, easy color reading and sensing reliability under ambient conditions must be addressed. The former two aspects were recently discussed.^[37,39,40] Using the concept of supermodules QR codes^[37,41] designed to avoid the overlap of emission colors (and rendering easier decoding), distinct security levels were assured through UV illumination (first level) and encrypted information securely transmitted to a server or database (second level).^[37] However, although security and color demultiplexing limitations are overcome using this multiplexing scheme of QR codes, temperature sensing was not explored yet.

In this work, we further explore the optical features of two noncontacting aqueous and plastic inks doped with judiciously chosen lanthanides ($\text{Ln}^{3+} = \text{Eu}^{3+}$ and Tb^{3+}) complexes comprising suitable ligands. Pure color emission (full width at half maximum, fwhm < 4 nm) in the red (Eu^{3+}) and green (Tb^{3+}) spectral regions and excellent photo- and chemical stabilities were demonstrated upon accelerated aging tests conducted under

controlled relative humidity and temperature and prolonged continuous solar irradiation (AM1.5G , 1000 W m^{-2}).^[37] Two QR codes based on a conventional black/white QR code and a luminescent QR code with customized smart location patterns were stamped on a medical adhesive. These smart labels provide trackability and three synchronous and independent temperature readouts based on photographs taken with a smartphone. As an added benefit, the thermal optical properties of the dual $\text{Tb}^{3+}/\text{Eu}^{3+}$ intra-4f emission intensities, thermometric parameters, and thermal sensitivity were theoretically modeled using density functional theory (DFT), through its time-dependent approach (TD-DFT),^[42] intramolecular energy transfer (IET),^[43] and rate equations.^[44] This theoretical modeling furnishes directions for further improvements in what concerns the design of luminescent inks with tailored color emission and thermal dependence toward smarter and personalized IoT medical devices for eHealth and mHealth.

2. Results and Discussion

2.1. Customized QR Codes' Design and Optical Properties

Medical adhesives were used to print customized luminescent QR codes designed for trackability, authentication, security, and sensing (Figure 1). The black/white QR code is accessed under ambient illumination and can be easily scanned with the user's mobile device, providing a link to an internet server containing static information (e.g., medical or directions for use typically printed on the adhesive box). Under light emitting diodes (LEDs) excitation, a luminescent QR code formed by red-emitting (Eu^{3+}) smart location patterns and green-emitting modules (Tb^{3+}) becomes visible. The red color (location patterns) and the green one (modules) arise from the optical features of $\text{Eu}^{3+}/\text{Tb}^{3+}$ -doped organic–inorganic inks. The hybrid host (termed diureasil^[38]) is formed by polyether chains covalently bonded to a siliceous skeleton (Figure S1a, Supporting Information). The ink incorporating Eu^{3+} and Tb^{3+} will be hereafter termed dU6Eu and dU6Tb, respectively.

The luminescent smart QR codes are able to store unique authentication tags,^[37] that can be securely transmitted to a remote server, which enables the trackability and the triggering of security alerts or other additional security features (dU6Tb and dU6Eu, Figure 1). In simultaneous, the combination of the green and red emissions will permit the temperature measurement through three independent readouts (thermometric parameters Δ_{1-3} , Figure 1). Moreover, and as an added benefit, Δ_3 is theoretically predicted based on energy transfer processes.

Following this strategy, Figure 2 shows photographic records of the customized QR codes under natural daylight (Figure 2a,b) and UV radiation (Figure 2c,d) printed on a commercial medical adhesive. We note the remarkable mechanical properties of aqueous-based inks (Figure S2–S8, Supporting Information), endorsed by the flexibility of the printed optical sensors (Figure S8, Supporting Information). As an added benefit, the multiplexed QR codes display a two-fold storage capacity (compared with that of the conventional ones).^[45] Individual luminescent QR codes printed on a plastic substrate (acetate) were also fabricated.^[13]

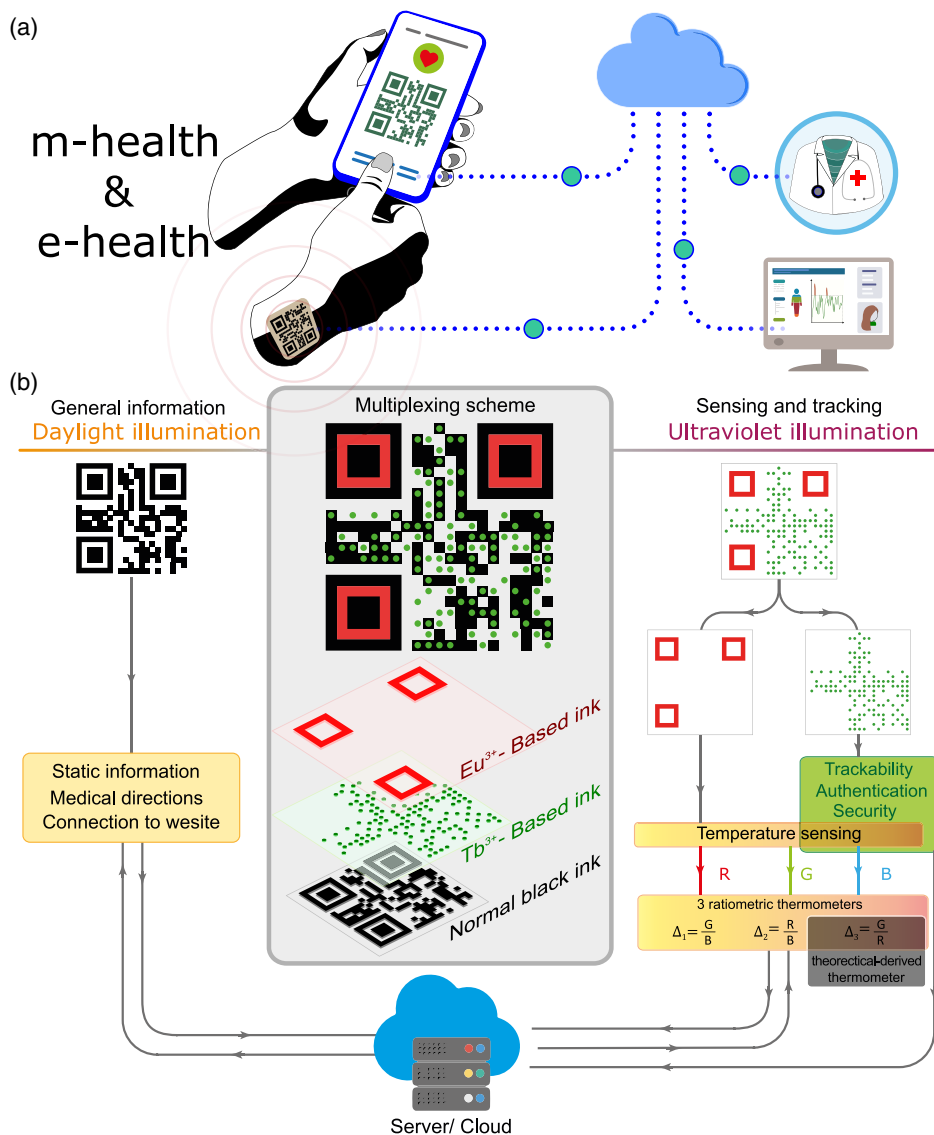


Figure 1. Schematic of the proposed QR codes based on luminescent modules (dU6Tb) and smart location patterns (dU6Eu). The QR code contains three independent temperature readouts due to the use of two distinct inks (color multiplexing). The combined use of dU6Eu and dU6Tb enables the addition of a theoretical-derived thermometric parameter. The use of dedicated applications/devices permits monitoring and security through an encrypted connection to a server.

These intriguing properties of the selected inks benefit from the judicious choice of Ln^{3+} complexes and of its interaction with diureasil host, as detailed in Supporting Information. The red and green emission colors arise from the intra- $4f^6$ (dU6Eu) and intra- $4f^8$ (dU6Tb) transitions, as shown in Figure 2e,f. For the latter, low-relative intensity broadband in the blue spectral region ascribed to diureasil intrinsic emission^[46] is also discerned (Figure 2g). This emission is ascribed to electron–hole recombination occurring in the siliceous backbone (Si) and on the urea (NH) crosslinkages.^[47,48] The temperature dependence of the emission of the dU6Tb QR code is perceptible to the naked eye (Figure S9, Supporting Information) due to the changes in the relative intensity between the intra- $4f^8$ transitions and the ureasil broadband (emission color variation within the

yellowish–green spectral region, Figure 2h). In the case of the dU6Eu QR code, only the intra- $4f^6$ transitions are discerned, whose energy is independent of the temperature, yielding a constant color in the temperature range (298–314 K) lying in the red pure color region of the chromaticity diagram.

As the emission intensity and color are strongly influenced by the contribution (dU6Tb) or absence (dU6Eu) of the diureasil blue component, we modeled the red (Eu^{3+}) and green (Tb^{3+}) components using DFT and IET theory^[43] and the rate equations^[44] (Section 4 in Supporting Information for details). The diureasil emission intensity was not modeled because although the diureasil emitting level populations were included in the rate equations, the nonradiative energy transfer from the diureasil emitting levels to the ligand triplet states induces very low

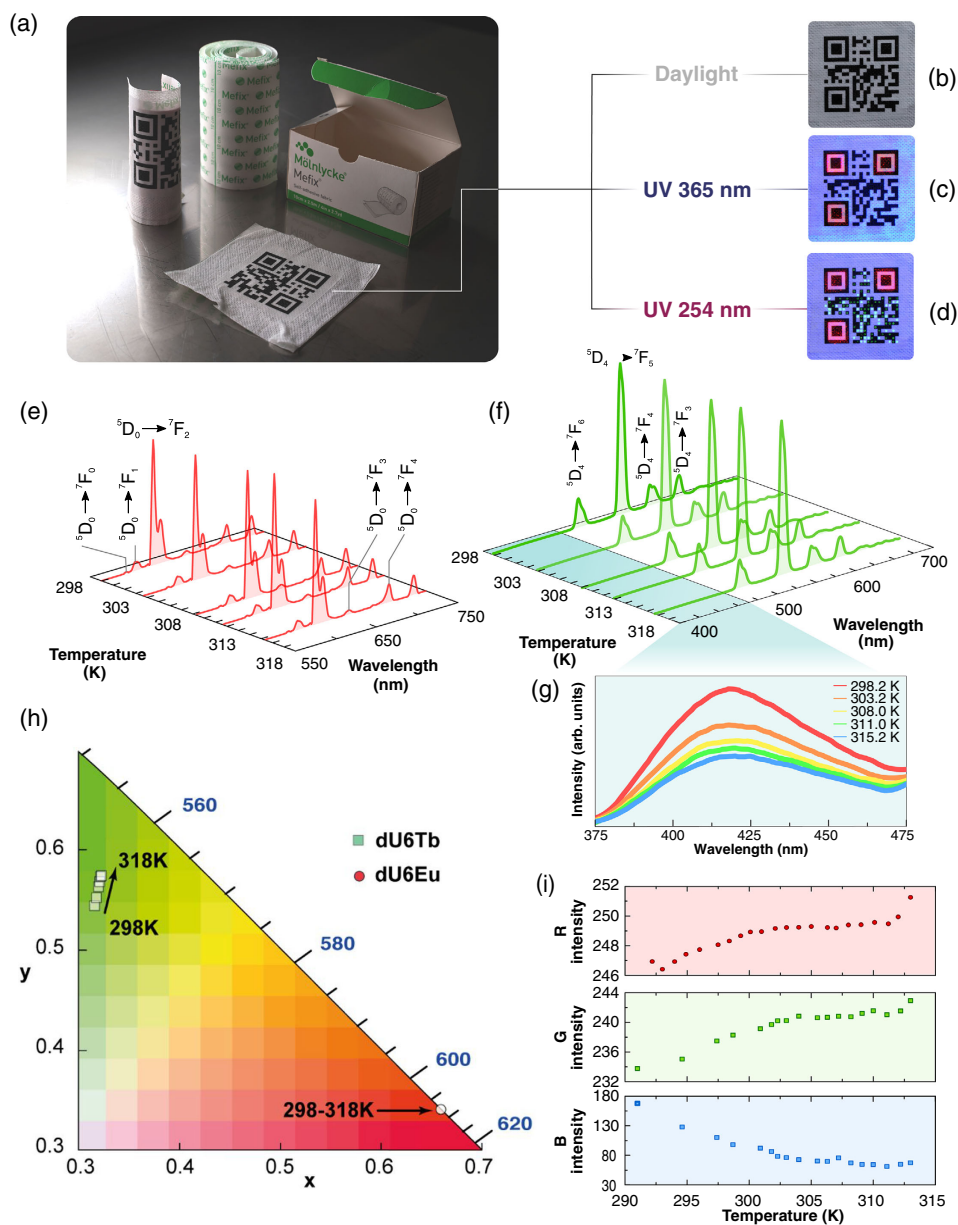


Figure 2. a–d) Photographic records of the customized QR codes printed in a medical adhesive under daylight and UV illumination. Emission spectra excited at 365 nm in the range 298–318 K for e) dU6Eu and f) dU6Tb QR codes; g) magnification ($\times 40$) in the 375–475 nm for dU6Tb. h) Partial CIE chromaticity diagram for the emission color dependence on the temperature. i) Absolute intensity of the R (dU6Eu), G, and B (dU6Tb) coordinates and R coordinate absolute value (ranging from 0 to 255) in the 294–313 K temperature range.

populations. Therefore, emphasis was given to the Ln^{3+} -based emission modeling.

The DFT and TD-DFT provide us the necessary data (such as molecular structure and the centroid of the low-energy lying donor singlet (S_1) and triplet (T_1) states in each complex, Figure S13 and S14, Supporting Information) to proceed with the IET calculations. The intersystem crossing rate $S_1 \rightarrow T_1$ (W_{ISC}) is sensitive to the energy gap between the S_1 and T_1 state,^[49] being 8063 cm^{-1} (dU6Eu) and 6507 cm^{-1} (dU6Tb) and leading to non-negligible values of $W_{\text{ISC}} \approx 10^5 \text{ s}^{-1}$ and 10^6 s^{-1} , respectively.^[50–52] The observation of the ureasil-related band

in dU6Tb is ascribed to higher backward energy transfer rates from Tb^{3+} levels to the hybrid moieties ($W_{\text{b}}^{\text{NH}} = 1.15 \times 10^9 \text{ s}^{-1}$ and $W_{\text{b}}^{\text{Si}} \approx 3.62 \times 10^5 \text{ s}^{-1}$ and backward pathways 47–88 in Table S5, Supporting Information, than the forward ones ($W^{\text{NH}} \approx 8.56 \times 10^5$ and $W^{\text{Si}} \approx 9.28 \times 10^3 \text{ s}^{-1}$, forward pathways 47–88 in Table S5, Supporting Information). Also, the decrease in the ureasil band intensity when temperature increases is corroborated by the population fraction reduction of the Si and NH moieties (Figure S16, Supporting Information). In contrast, in the case of dU6Eu, the diureasil band is absent due to the lower backward energy transfer rates from the Eu^{3+} levels to the hybrid

moieties ($W_b^{NH} = 2.80 \times 10^7 \text{ s}^{-1}$ and $W_b^{Si} \cong 1.24 \times 10^4 \text{ s}^{-1}$, backward pathways 35–64 in Table S6, Supporting Information), together with an enhancement of the forward ones ($W^{NH} \cong 5.13 \times 10^8 \text{ s}^{-1}$ and $W^{Si} \cong 6.84 \times 10^4 \text{ s}^{-1}$, forward pathways 35–64 in Table S6, Supporting Information). The lower backward energy transfer rates and the higher forward ones observed for dU6Eu, compared with dU6Tb, are rational for the experimental evidence concerning the presence of radiative emission from the diureasil excited states only in the presence of the Tb^{3+} -based complex.

These optical features enable the correlation of the emission spectra thermal dependence with the color coordinates in the 1931 Commission Internationale d'Éclairage (CIE) XYZ and red, blue, and green (RGB) color spaces, using the QR codes' photographs taken with a smartphone. The dU6Eu and dU6Tb emission spectra overlap the CIE color-matching functions termed \bar{x} , and \bar{y} , \bar{z} , respectively (Figure S10, Supporting Information), which are mathematical transformations from 1931 CIE RGB color-matching functions (Figure S11, Supporting Information). Attending to the larger overlap of the intra- $4f^6$ (dU6Eu) and intra- $4f^8$ (dU6Tb) transitions with the R and G components (92% and 76%, respectively), those were used to quantify the emission dependence on the temperature. The B channel corresponds to the contribution of the diureasil emission in the case of dU6Tb. For this label, the intensity of G increases, whereas the B channel intensity decreases as the temperature increases (Figure 2i). For the dU6Eu QR code, the R channel intensity increases as observed for the R component,

in the 294–314 K range. (Figure 2i). An analogous trend was observed for the integrated intensity of the intra- $4f^6$ (dU6Eu) and intra- $4f^8$ (dU6Tb) transitions (Figure S12, Supporting Information), reinforcing that the R and G components are good choices to quantify the thermal emission intensity dependence.

The measured color change is an opportunity to build a sensor for mHealth including IoT based on the RGB color coordinates from images acquired with a smartphone, avoiding the use of expensive and less accessible equipment. This allows the definition of different thermometers within the same label to work together to improve the reliability through the temperature sensing using independent readouts based on single QR codes and combining the emission features of distinct labels (modules and location patterns). To achieve such a goal, three ($i = 1-3$) thermometric parameters (Δ_i) are defined (Equation (1), Figure 3 and 5).

$$\begin{cases} \Delta_1 = \frac{G}{B} \\ \Delta_2 = \frac{B}{G} \\ \Delta_3 = \frac{G}{R} \end{cases} \quad (1)$$

Using only the dU6Tb layer, Δ_1 is based on the ratio between G and B. Combining the dU6Tb with the dU6Eu, two extra parameters are defined (Δ_2 and Δ_3). One setting as reference the R component (dU6Eu) in combination with B from dU6Tb (Δ_2) and another using as the R component (dU6Eu) and G from dU6Tb (Δ_3). These are independent ratiometric thermometers

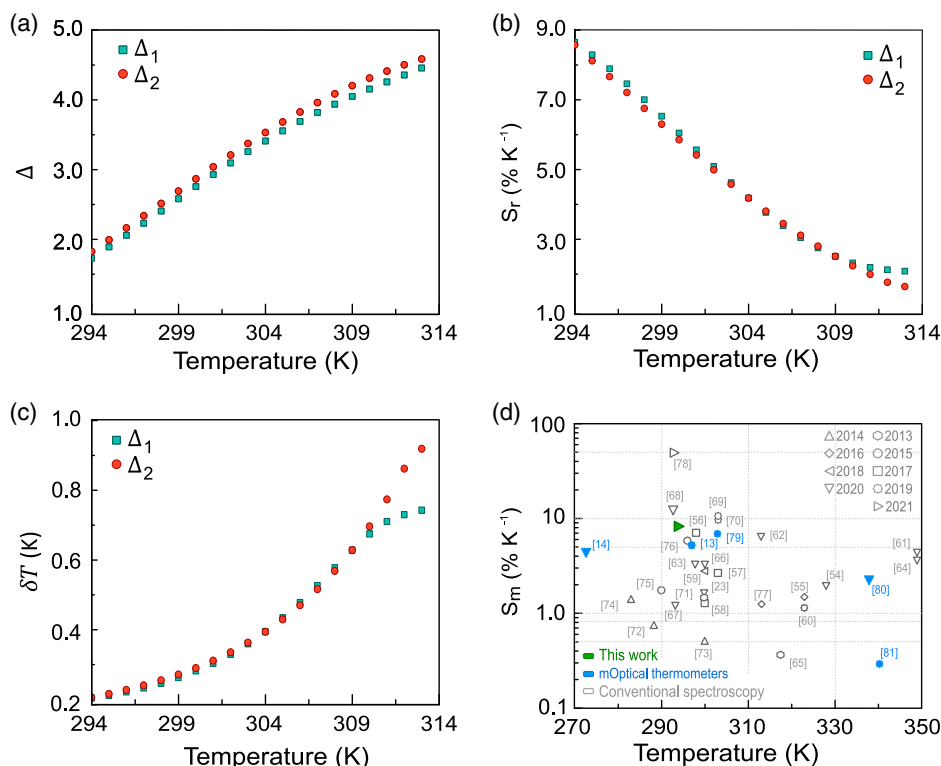


Figure 3. a) Thermometric parameters in the 294–313 K range. b) Relative thermal sensitivity, c) temperature uncertainty, and d) maximum relative sensitivity values reported in the literature presenting a comparison between luminescent thermometers based on conventional spectroscopy, inserted into IoT, and the ones presented in this work.

whose performance is typically evaluated using the relative sensitivity and the temperature uncertainty (Section S3, Supporting Information, for more details).^[53] Calculation of relative sensitivity requires the differentiation of Δ for temperature; here, a simple two-point numerical differentiation was used, yielding both a maximum relative thermal sensitivity (S_m) of $8.5\% \text{ K}^{-1}$ at 294 K and a minimum temperature uncertainty (δT) of 0.18 at 294 K (Figure 3b,c). The comparison of S_m with data reported in the literature is shown in Figure 3d. Such comparison includes the figures of merit from conventional spectroscopic^[23,54–78] and mOptical sensing for IoT.^[13,14,79–81] Noticeably, the figures of merit reported here are among the best ones in the literature, demonstrating the potential of color demultiplexing^[45] to push luminescence thermometry toward IoT in a simple way.

We note that such figures of merit although useful to distinguish some medical situations, such as the monitoring of injured or wound body locations, where the temperature variation that may indicate the presence of an infection is usually about 1°C ,^[82] are less suitable to establish a fever status. As fever is determined in a shorter temperature range ($37.8\text{--}40.0^\circ\text{C}$),^[83,84] the typical S_m and δT values reported so far in such a narrow range may lead to false positives, false negatives, or inconclusive results, being unsatisfactory for some medical applications. In fact, the improvement of S_r and δT values for physiological temperatures was recognized as one of the main challenges of the emerging field of luminescent micro- and nanothermometry.^{[19][53][85]} and a recent breakthrough in this direction reporting a tenfold improvement in S_r and δT in that temperature range, reaching a world record of $50\% \text{ K}^{-1}$ and 0.05 K, respectively.^[78]

In the next section, we will provide theoretical modeling for Δ_3 , allowing the temperature readout based on the R and G components to be independently verified through theoretical modeling. This permits to infer degradation of the medical adhesive as a smart label because the R and G coordinates arise from dU6Eu and dU6Tb inks, respectively. Therefore, any deviation between the predicted temperature through Δ_3 using the ratiometric and the theoretical-derived thermometer approaches is evidence that the medical adhesive is damaged and should be replaced. We also notice that the temperature readout is conducted in a short time interval (1/10 s), disabling, therefore, any potential effect of illumination on sample heating, even if prolonged exposure time in real applications is expected as one of the QR code features is the fast-reading time.

2.2. Theoretical Modeling of the R/G Luminescent Thermometer

Typically, when characterizing a luminescent thermometer, the Δ values would be used to adjust a fitting curve that describes the variation in the full temperature range (termed calibration curve). When lacking a well-defined and well-known theoretical model, an empirical (and most of the cases generic) equation is used. It can be argued that in some scenarios this does not bring much value other than describing the temperature dependence of the Δ parameter. Furthermore, this procedure could even lead to the introduction of artifacts in the evaluation of the thermometer figures of merit due to the miss-fitting procedure. From the theoretical point of view, we can rationalize the thermometric parameter $\Delta_3 = G/R$, establishing how the IET rates involving Ln^{3+} ions may

define the populations of $^5\text{D}_4$ (Tb^{3+}) and $^5\text{D}_0$ (Eu^{3+}) emitting levels when the temperature changes (see Section S4 and S5, Supporting Information, for more details).

To conduct the theoretical modulation, two experimental sets of data are required, namely, the molecular structure of dU6Ln ($\text{Ln} = \text{Tb}, \text{Eu}$) and the experimental lifetime of the excited emitting states. Therefore, the photophysical properties of the flexible QR codes were further characterized as a function of the temperature

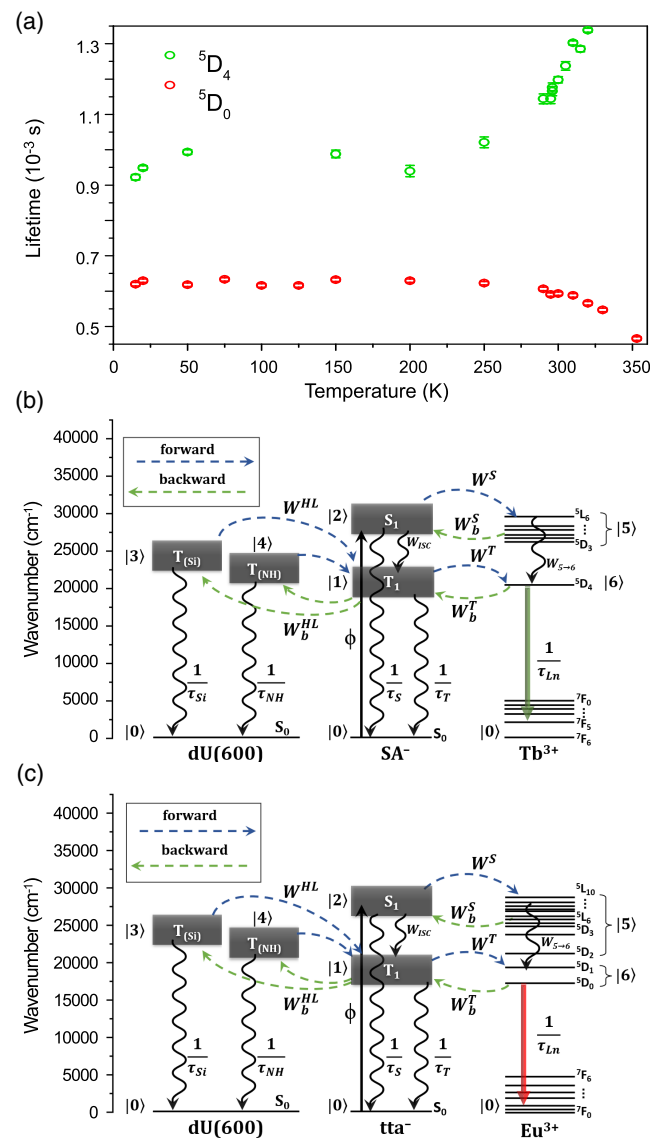


Figure 4. a) Temperature dependence of $^5\text{D}_4$ and $^5\text{D}_0$ lifetimes, excited at 365 nm and monitored at 543 and 612 nm, respectively. Jablonski-type energy level diagrams for b) dU6Tb and c) dU6Eu systems showing the levels, the decay rates, and the main IET rates involved (forward and backward). τ_T , τ_S , τ_{Si} , τ_{NH} , and τ_{Ln} are the lifetimes of T₁, S₁, Si, NH, and $^4\text{D}_4$, $^5\text{D}_0$ emitting levels. W^T , W^S , W^{NH} , and W^{Si} are the forward IET rates from the T₁, S₁, NH, and Si states to the Ln³⁺ ion, respectively, whereas W_{5-6} is the multiphonon decay rate from the Ln³⁺ upper levels to the emitting ones. The superscript HL indicates the hybrid-to-ligand rates from dU(600) moieties (NH and Si) to the ligands' (SA⁻ and tta⁻) T₁ and S₁ states. All the backward rates are indicated by a subscript b.

Table 1. Steady-state regime population of the ground and Ln³⁺ emitting levels for the dU6Tb and dU6Eu complexes in the 294–313 K range.

T [K]	dU6Tb		dU6Eu	
	N ₀	N ₆ (×10 ⁻¹)	N ₀	N ₆ (×10 ⁻¹)
294	0.9179	0.8200	0.9566	0.3729
295	0.9157	0.8420	0.9565	0.3735
296	0.9122	0.8776	0.9564	0.3742
297	0.9127	0.8720	0.9563	0.3749
298	0.9169	0.8300	0.9562	0.3756
299	0.9109	0.8904	0.9561	0.3763
300	0.9017	0.9826	0.9560	0.3769
301	0.9017	0.9820	0.9559	0.3776
302	0.8976	1.0230	0.9558	0.3783
303	0.8947	1.0522	0.9557	0.3790
304	0.8898	1.1015	0.9556	0.3796
305	0.8912	1.0874	0.9555	0.3803
306	0.8873	1.1265	0.9554	0.3809
307	0.9179	0.8200	0.9553	0.3816
308	0.9157	0.8420	0.9552	0.3823
309	0.9122	0.8776	0.9551	0.3830
310	0.9127	0.8720	0.9550	0.3836
311	0.9169	0.8300	0.9549	0.3843
312	0.9109	0.8904	0.9548	0.3849
313	0.9017	0.9826	0.9547	0.3856

by the measurement of the ⁵D₄ (dU6Tb) and ⁵D₀ (dU6Eu) lifetimes (τ_{Ln}) monitored in a large broad temperature interval (14–350 K, **Figure 4a**). All the decay curves are well modeled by a single exponential function, providing evidence that the ⁵D₀ lifetime remains stable up to 250 K (0.624 ± 0.002 × 10⁻³ s), decreasing to 0.466 ± 0.005 × 10⁻³ s at 350 K (**Figure 4a** and **Figure S6**, Supporting Information). The ⁵D₄ lifetime remains stable up to 200 K (1.10 ± 0.03 × 10⁻³ s), increasing to 1.353 ± 0.005 × 10⁻³ s at 350 K (**Figure 4a** and **Figure S7**, Supporting Information). However, the thermal dependence of the ⁵D₀ lifetime is typically observed in several complexes arising from compelling thermally activated nonradiative mechanisms.^[86,87] The ⁵D₄ lifetime increases uncommonly, demonstrating the active role of diureasil on the optical features of the inks. In particular, the dependence of the refractive index of the hybrid host on the temperature a high thermal optical coefficient (≈ -7 × 10⁻⁴ °C⁻¹),^[88] which directly contributes to a slight decrease in the radiative rate A_{rad} (also known as spontaneous emission coefficients, Equation S(21), Supporting Information). Furthermore, the ⁵D₄ nonradiative decay (A_{nrad}) is also decreased due to the higher nonradiative backward rate Tb³⁺ → T₁ (W_b^T = 1.30 × 10⁸ s⁻¹) than the forward T₁ → Tb³⁺ (W^T = 1.04 × 10⁶ s⁻¹), meaning that a parcel of non-radiative decay from ⁵D₄ is transferred to the salicylic acid T₁ state. The latter effect is not observed in the dU6Eu compound due to its W^T > W_b^T opposite condition for any temperature (**Table S6** and **Figure S15**, Supporting Information).

From the calculated IET rates, and Jablonski-type diagrams (**Figure 4b,c**), we may describe the global kinetics involved in each dU6Ln, simulating their intra-4f emissions (i.e., ⁵D₄ → ⁷F₅

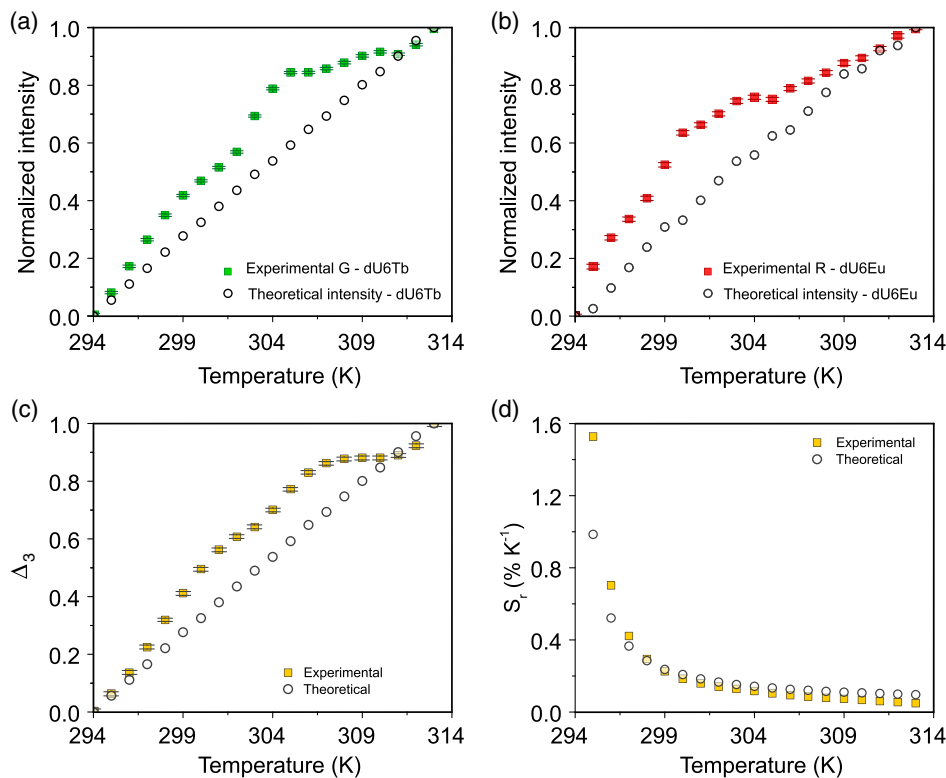


Figure 5. Normalized experimental G (dU6Tb) and R (dU6Eu) color coordinates retrieved from the images and theoretical intensities for a) dU6Tb and b) dU6Eu in the 294–313 K range. c) Thermometric parameter Δ₃ and d) relative sensitivity. The experimental and theoretical data are represented by filled squares and empty circles, respectively.

and ${}^5D_0 \rightarrow {}^7F_2$). The emitting level population in the steady-state regime and the comparison between experimental and theoretical values for the emission intensities (${}^5D_4 \rightarrow {}^7F_5$ and ${}^5D_0 \rightarrow {}^7F_2$) and the thermometric parameter Δ_3 are shown in Table 1 and S7, Supporting Information, respectively.

Figure 5 shows the good agreement between experimental and theoretical thermometric properties involving the G and R color coordinates, demonstrating that IET rates can be used to predict the performance of energy-driven luminescent thermometers. Moreover, this approach provides an extra tool for materials design and, in the present case, to establish a simple tool to determine the lifetime of the medical adhesive as a reliable sensor. The need for replacement is set when distinct temperature values of Δ_3 are indicated via the ratiometric approach (Equation (1)) and theoretical predictions, establishing a self-performance evaluation of the medical adhesive.

3. Conclusion

Luminescent QR codes based on the combination in a single material of a diureasil organic–inorganic host and Eu^{3+} and Tb^{3+} complexes were designed to develop a smart label medical adhesive. The QR codes were printed on commercial medical adhesive and the two independent layers and smart location patterns provide simultaneous tracking and multiple synching temperature readouts. The thermometers display three independent radiometric readouts, and the combined use of Eu^{3+} and Tb^{3+} enables the addition of a theoretical-derived thermometric parameter, using TD-DFT and IET as theoretical background. The modeling used here showed to be useful for prediction and allowed us to know which parameters can be modulated to improve the thermal response of R and G emission of the inks. This new theoretical methodology is a step toward a smart design of responsive QR codes for the IoT. Noticeably, this theoretical approach can be easily extended to other Ln-based materials featuring emission optimization in different areas behind sensing (lighting, photovoltaics, among others).

4. Experimental Section

The inks were based on organic–inorganic hybrids (diureasils),^[38] whose preparation occurred under ambient conditions and exclusively relied on “green” water-based methods.^[37] Such simple, fast, clean, and cheap processes will be sought, ideal in a scale-up scenario for industrial applications and its processing as QR codes ensure IoT for sensing applications for widespread sustainable use. Moreover, they combined the advantages of Ln^{3+} , such as long emission lifetimes (millisecond scale) and pure color emission. Also, Ln^{3+} stood out because of the well-known poor stability of organic dyes (natural or synthetic)^[89] and quantum dots (QDs), whose autofluorescence, scattering, and phototoxicity were unwanted for large societal widespread.^[90] The temperature was measured based on the thermal dependence of the emission color of codoped lanthanide ($\text{Ln}^{3+} = \text{Eu}^{3+}$, Tb^{3+})-based organic–inorganic hybrids.

Materials and Synthesis: α,ω -diaminepoly(oxyethylene-co-oxypropylene) (ED-600, Huntsman), 3-isocyanatopropyltriethoxysilane (ICPTES, 95%, Aldrich), 2-thenoyltrifluoroacetone (Htta, Sigma-Aldrich), salicylic acid (SA, Acofarma, Spain), and $\text{EuCl}_3 \cdot 6\text{H}_2\text{O}$ (Aldrich) were commercially available. Terbium chloride (TbCl_3) aqueous solution (0.2 mol L^{-1}) was obtained by dissolving terbium oxide (Tb_4O_7 , Yuelong New Material Co., Ltd., Shanghai, China) in hydrochloric acid (HCl, 37%, Aldrich). Tetrahydrofuran (THF) and absolute ethanol (EtOH) were used as solvents. HCl (0.05 mol L^{-1}) and sodium hydroxide (NaOH , 1.0 mol L^{-1}) aqueous solutions were used for the sol–gel reaction and Tb complex

formation. All chemicals were used as received without purification. Distilled water was used throughout the experiments.

Synthesis of the Complexes $\text{Eu}(\text{tta})_3(\text{H}_2\text{O})_2$ and TbSA : $\text{Eu}(\text{tta})_3(\text{H}_2\text{O})_2$ (Figure S1b, Supporting Information) was synthesized by reaction of $\text{EuCl}_3 \cdot 6\text{H}_2\text{O}$ and tta in the presence of NaOH ethanol solution with the molar ratio of $\text{EuCl}_3 \cdot 6\text{H}_2\text{O}:\text{tta}:\text{NaOH} = 1:3:3$ according to the method described in the study by Melby et al.^[91] Elemental analysis results were in good agreement with the proposed formula of $\text{Eu}(\text{tta})_3 \cdot 2\text{H}_2\text{O}$. Calcd. (%) for $\text{C}_{24}\text{H}_{16}\text{EuF}_9\text{O}_8\text{S}_3$: C 33.85, H 1.89, and S 11.30; found: C 33.73, H 1.81, and S 11.88. The TbSA complex was synthesized by reaction of TbCl_3 with SA in the mixed solution of EtOH and water.

Synthesis of the dU6Eu Ink: The organic–inorganic hybrid precursor d-UPTES(600) (Figure S1a, Supporting Information) was prepared by reaction of ED-600 and ICPTES using THF as the solvent according to the procedure published previously.^[38] The dU6Eu ink was prepared by mixing 50 mg of $\text{Eu}(\text{tta})_3(\text{H}_2\text{O})_2$ dissolved in 10 mL of EtOH and 5.0 g of d-UPTES(600) under stirring. The dU6Eu ink (sol) was also dried to obtain dU6Eu gel.

Synthesis of the dU6Tb Ink: dU6Tb ink was prepared according to our previous protocol with some modifications.^[37,92] Typically, 1.371 mL (0.274 mmol) of TbCl_3 aqueous solution was added to a beaker and dried to evaporate the water. Then, 1.0 g (0.913 mmol) of d-UPTES(600) was added, followed by the addition of 5 mL of absolute ethanol. The mixture was stirred at room temperature to get a clear solution. Then, 0.098 mL of 0.05 mol L^{-1} HCl was added and stirred at room temperature for 30 min. 113.6 mg (0.821 mmol) of SA was added, stirred for some time, and finally, 0.823 mL of 1.0 mol L^{-1} NaOH aqueous solution was added under stirring. The molar ratio of d-UPTES(600): TbCl_3 :SA:NaOH was 1:0.3:0.9:0.9. The above mixture was stirred at room temperature for a while and dU6Tb ink was obtained. The dU6Tb ink (sol) was also dried to afford dU6Tb gel. The viscosities of dU6Eu and dU6Tb were measured on Brookfield DV-II + Pro Viscometer at room temperature, and the values were 4.89 and 4.51 mPa s for dU6Eu and dU6Tb, respectively.

QR Code Processing: The dU6Tb and dU6Eu QR codes were generated with the message “TEMP=”, resulting in a version 1 QR code with an error correction level of 7%. The luminescent QR codes were produced on a 5.0×10^{-4} m-thick acetate substrate layer, laser cut into the QR code shape (the region of the inactive modules was removed), and afterward coated with dU6Tb and dU6Eu inks. After deposition, the substrates with the luminescent QR codes were transferred to an oven at 45°C for 48 h. As proof of concept for biomedical applications, a black/white QR code was transferred to a medical adhesive using a stamping process. The QR code was printed on transfer paper (Transfer Paper Inkjet Light A4) and transferred to the medical adhesive using a heat press. The luminescent material was deposited on top of the black/white QR code using an airbrush technique. The luminescent QR codes’ design in the medical adhesive was achieved using an acetate mask with a dot-shaped QR code. To ensure reproducibility, around 50 QR codes were printed with different dimensions, modules, and location pattern types using distinct deposition techniques. There is no evidence that the QR codes processing induces any change in the thermal sensitivity, as the luminescence ratio intensity is not affected.

Emission Spectra and Photographic Records: The QR code response to temperature was calibrated using the emission spectra and the smartphone photographic records of the QR codes under UV excitation (Spectroline ENF-280C/FE, 365 nm). Temperature control was made with a homemade Peltier plate-based temperature controller and a K-type thermocouple. After setting a temperature in the controller, the QR code was let to thermalize for ≈ 5 min. As reported previously this acquisition setup configuration ensured temperature uniformity within the QR code.^[13] The temperature-dependent emission spectra of the QR codes were measured using a portable spectrometer (OceanOptics Maya 2000 Pro with an integration time of 250 ms) coupled with an optical fiber placed at a central location of the code. After the acquisition of a spectrum, photographic records of the QR codes were taken with a smartphone camera.

Image Processing: The photographic records of the QR codes were captured with a Sony ILCE-7M3 with a sensor CMOS Exmor R (35 mm full frame) and also with an unchanged available smartphone with a resolution $4160 \times 3120 \text{ pixel}^2$, an aperture of $f/1.9$, and sensor dimension of $1/2.6''$,

using a commercially available camera app that allows locking all the settings and ensuring the same conditions during the experiment. The images were acquired with an exposure time of 1/10 s. The color coordinates from the photographs were determined using the RGB model.^[13,93]

RGB Color Model: The RGB color model is an additive model that generates each color by mixing unique quantities of the three primaries red, green, and blue. Know that each color is composed of a unique set of RGB coordinates and it is possible to reverse the process and obtain the original primary values. Based on this, every image in this color model can be decomposed into three separated images (one corresponding to a channel). Each image was analyzed by an intensity histogram (considering the intensity of all pixels in the image) fitted by a Gaussian probability density function (pdf). From the fit, it was possible to separate the luminescent contribution from the nonluminescent. Also, it was possible to extract the R, G, and B values for luminescent material, which were the values obtained from the associated pdf.^[13,93]

Theoretical Simulations: The molecular geometry optimizations of dU6Ln (Ln: Tb and Eu) were calculated using the Gaussian 09 program^[94] with B3LYP functional.^[95,96] The basis set 6-31 G(d) was used and the Ln³⁺ ions were treated with MWB52 (Eu³⁺) and MWB54 (Tb³⁺).^[97] The TD-DFT was conducted using the optimized structure and the same functional and basis set as mentioned before. The intensity parameters were obtained using the simple overlap model^[98] (SOM) for the ligand field and the bond overlap model^[99,100] (BOM) for the ligand–polarizability dependent term in the JOYSpectra program.^[101] The IET rates were calculated according to the approach described in the literature.^[43,102–104] The kinetics of an IET process included an equilibrium involving the absorption, IET (both forward and backward energy transfer), radiative and nonradiative decay rates involving the donor moieties (NH/Si of the hybrid; S₁/T₁ of the main ligands SA[−] and tta[−]), and Ln³⁺-ion states. This kinetics was described by an appropriate system of rate equations for a hybrid ligand–Ln³⁺ unit; the ensemble of these factors enabled the description of macroscopic photophysical properties such as Ln³⁺ emission.

Figure 4 shows the simplified energy-level diagrams for the dU6Tb and dU6Eu compounds. All effective energy transfer channels are illustrated, showing the complexity of a seven-level energy-level diagram. The population of a state $|n\rangle$ was addressed as N_n , and taking into consideration, in the independent systems model, the populations of each system were normalized ($\sum N_n = 1$). Under these conditions, a seven-level system composed of ordinary differential equations (ODEs) is given by

$$\frac{dN_0}{dt} = \frac{1}{\tau_T} N_1 + \frac{1}{\tau_S} N_2 + \frac{1}{\tau_{Si}} N_3 + \frac{1}{\tau_{NH}} N_4 + \frac{1}{\tau_{Ln}} N_6 - \varphi N_0 \quad (2)$$

$$\frac{dN_1}{dt} = W_{ISC} N_2 + W^{Si-T} N_3 + W^{NH-T} N_4 + W_b^T N_6 - \left(\frac{1}{\tau_T} + W^T + W_b^{NH-T} \right) N_1 \quad (3)$$

$$\frac{dN_2}{dt} = \varphi N_0 + W_b^S N_5 - \left(\frac{1}{\tau_S} + W_{ISC} + W_b^{Si-S} + W_b^{NH-S} \right) N_2 \quad (4)$$

$$\frac{dN_3}{dt} = W_b^{Si-S} N_2 + W_b^{Si} N_5 - \left(\frac{1}{\tau_{Si}} + W^{Si-T} + W^{Si} \right) N_3 \quad (5)$$

$$\frac{dN_4}{dt} = W_b^{NH-T} N_1 + W_b^{NH} N_5 + W_b^{NH-S} N_2 - \left(\frac{1}{\tau_{NH}} + W^{NH-T} + W^{NH} \right) N_4 \quad (6)$$

$$\frac{dN_5}{dt} = W^S N_2 - (W_{5-6} + W_b^S + W_b^{NH} + W_b^{Si} + W_b^T) N_5 \quad (7)$$

$$\frac{dN_6}{dt} = W^T N_1 + W^{Si} N_3 + W^{NH} N_4 + W_{5-6} N_5 - \left(\frac{1}{\tau_{Ln}} + W_b^T \right) N_6 \quad (8)$$

The rate enters in Equation (7) for the Tb³⁺ and Equation (8) for the Eu³⁺ compound once the backward rates W_b^T (T₁→Ln³⁺) are owed to the

level N₆ for Eu³⁺ (⁵D₀ and ⁵D₁) and to N₅ for Tb³⁺ (upper levels). For example, the backward energy transfer from the Tb³⁺ emitting level (⁵D₄) to T₁ is in the order of $\approx 10^{-2} \text{ s}^{-1}$ (see pathway 26, Table S5, Supporting Information); thus, the Tb³⁺ upper levels (N₅) are responsible for the rate $W_b^T \approx 10^8 \text{ s}^{-1}$ (see pathways 28 and 41 in Table S5, Supporting Information); then, W_b^T should be considered only in Equation 7 for dU6Tb, whereas, for the dU6Eu case, W_b^T is considered only in Equation (8).

τ_T , τ_S , τ_{Si} , τ_{NH} , and τ_{Ln} are the lifetimes of T₁, S₁, Si, NH, and Ln³⁺ emitting levels, respectively. In our simulations, $\tau_T = 1 \times 10^{-3} \text{ s}$, $\tau_S = 1 \times 10^{-9} \text{ s}$, $\tau_{Si} = 1.19 \times 10^{-5} \text{ s}$, and $\tau_{NH} = 4.87 \times 10^{-6} \text{ s}$ lifetimes were assumed as constants with the temperature once these decay rates affected the thermal behavior of Tb³⁺ and Eu³⁺ emitting level populations less,^[36] Tb³⁺ and Eu³⁺ being more dependent on the IET (forward and backward rates) and the τ_{Ln} lifetime. τ_T and τ_S are typical values found in the literature,^[105–107] whereas τ_{Si} and τ_{NH} were measured for the dU6Tb at 300 K (not shown).^[108] W_{ISC} is the intersystem crossing rate S₁ → T₁, which is sensitive to the energy gap between the S₁ and T₁ state.^[49] The energy gap of 8063 (for the Eu³⁺ compound) and 6507 cm^{−1} (for the Tb³⁺ compound) lead to a reasonable value of $W_{ISC} \approx 10^5$ and 10^6 s^{-1} .^[50–52] $W_{5-6} \approx 10^6 \text{ s}^{-1}$ is the decay rate from Ln³⁺ upper levels to the emitting ones for Ln³⁺-based chelates.^[43] W^S and W^T are the forward ligand-to-Ln energy transfer rates from the S₁ and T₁ states, respectively. The superscripts NH-T, Si-T, NH-S, and Si-S indicate the hybrid-to-ligand rates from dU(600) moieties (NH and Si) to the ligands' (SA[−] and tta[−]) T₁ and S₁ states. In all cases, the backward rates are indicated by a subscript b. W_{5-6} multiphonon decay rates (from Ln³⁺ upper levels to the emitting ones) are of the order of 10^6 s^{-1} .^[43] Based on the energy gap law and with the formalism of Miyakawa–Dexter's approach,^[109] we present estimations that these rates are reasonable for Ln³⁺-based chelates, as considered in the study by Carneiro Neto et al.^[43] (see Section S5.4, Supporting Information, for further details).

The set of rate equations (Equation (2)–(8)) was numerically solved using the Radau method.^[110] Each simulation from 0 to 20 ms was done in a step size of 2 μs, resulting in 10⁴ calculated points. Table 1 shows, in the operating temperature range 294–313 K, the normalized populations in the steady-state regime for the ground (N₀) and the Ln³⁺ emitting levels (N₆).

Supporting Information

Supporting Information is available from the Wiley Online Library or from the author.

Acknowledgements

This work was developed within the scope of the project CICECO-Aveiro Institute of Materials (UIDB/50011/2020 and UIDP/50011/2020), Instituto de Telecomunicações (FCT ref. UID/EEA/50008/2020), WinLEDs (POCI-01-0145-FEDER-030351), and Graphsense (POCI-01-0145-FEDER-032072) financed by national funds through the FCT/MEC and when appropriate cofinanced by FEDER under the PT2020 Partnership through European Regional Development Fund (ERDF) in the frame of Operational Competitiveness and Internationalization Programme (POCI).

Conflict of Interest

The authors declare no conflict of interest.

Data Availability Statement

Data available on request from the authors.

Keywords

eHealth, internet of things, lanthanides, luminescence, optical sensors, quick response codes, smartphones, temperature sensing

Received: July 14, 2021

Revised: September 13, 2021

Published online: November 9, 2021

- [1] G. Aceto, V. Persico, A. Pescapé, *J. Ind. Inf. Integr.* **2020**, *18*, 100129.
- [2] H. Elazhary, *J. Netw. Comput. Appl.* **2019**, *128*, 105.
- [3] S. Cai, X. Xu, W. Yang, J. Chen, X. Fang, *Adv. Mater.* **2019**, *31*, 1808138.
- [4] A. K. Yetisen, J. L. Martinez-Hurtado, B. Ünal, A. Khademhosseini, H. Butt, *Adv. Mater.* **2018**, *30*, 1706910.
- [5] R.-Q. Li, D.-W. Zheng, Z.-Y. Han, T.-Q. Xie, C. Zhang, J.-X. An, R. Xu, Y.-X. Sun, X.-Z. Zhang, *Mater. Today* **2020**, *40*, 91.
- [6] F. Ali, S. El-Sappagh, S. M. R. Islam, A. Ali, M. Attique, M. Imran, K.-S. Kwak, *Futur. Gener. Comput. Syst.* **2021**, *114*, 23.
- [7] S. Yao, P. Swetha, Y. Zhu, *Adv. Healthc. Mater.* **2018**, *7*, 1700889.
- [8] Y. Khan, A. E. Ostfeld, C. M. Lochner, A. Pierre, A. C. Arias, *Adv. Mater.* **2016**, *28*, 4373.
- [9] K.-D. Gruner, *Principles of Non-Contact Temperature Measurement*, Raytek Company, Berlin **2003**.
- [10] J. F. C. B. Ramalho, L. D. Carlos, P. S. André, R. A. S. Ferreira, *Adv. Photonics Res.* **2021**, *2*, 2000211.
- [11] R. Moreddu, M. Elsherif, H. Butt, D. Vigolo, A. K. Yetisen, *RSC Adv.* **2019**, *9*, 11433.
- [12] P. Kumbhakar, A. Roy Karmakar, G. P. Das, J. Chakraborty, C. S. Tiwary, P. Kumbhakar, *Nanoscale* **2021**, *13*, 2946.
- [13] J. F. C. B. Ramalho, S. F. H. Correia, L. Fu, L. L. F. António, C. D. S. Brites, P. S. André, R. A. S. Ferreira, L. D. Carlos, *Adv. Sci.* **2019**, *6*, 1900950.
- [14] N. Katumo, G. Gao, F. Laufer, B. S. Richards, I. A. Howard, *Adv. Opt. Mater.* **2020**, *8*, 2000507.
- [15] W. Piotrowski, K. Trejgis, K. Maciejewska, K. Ledwa, B. Fond, L. Marciniak, *ACS Appl. Mater. Interfaces* **2020**, *12*, 44039.
- [16] J. Othong, J. Boonmak, F. Kielar, S. Youngme, *ACS Appl. Mater. Interfaces* **2020**, *12*, 41776.
- [17] C. D. S. Brites, P. P. Lima, N. J. O. Silva, A. Millán, V. S. Amaral, F. Palacio, L. D. Carlos, *Nanoscale* **2012**, *4*, 4799.
- [18] D. Jaque, F. Vetrone, *Nanoscale* **2012**, *4*, 4301.
- [19] C. D. S. Brites, S. Balabhadra, L. D. Carlos, *Adv. Opt. Mater.* **2019**, *7*, 1801239.
- [20] M. D. Dramićanin, *J. Appl. Phys.* **2020**, *128*, 040902.
- [21] A. M. P. Botas, C. D. S. Brites, J. Wu, U. Kortshagen, R. N. Pereira, L. D. Carlos, R. A. S. Ferreira, *Part. Part. Syst. Charact.* **2016**, *33*, 740.
- [22] L. Labrador-Pérez, M. Pedroni, A. Speghini, J. García-Solé, P. Haro-González, D. Jaque, *Nanoscale* **2018**, *10*, 22319.
- [23] M. Suta, Ž. Antić, V. Đorđević, S. Kuzman, M. D. Dramićanin, A. Meijerink, *Nanomaterials* **2020**, *10*, 543.
- [24] Y. Shen, J. Lifante, N. Fernández, D. Jaque, E. Ximendes, *ACS Nano* **2020**, *14*, 4122.
- [25] X. Qiu, Q. Zhou, X. Zhu, Z. Wu, W. Feng, F. Li, *Nat. Commun.* **2020**, *11*, 4.
- [26] A. D. Pickel, A. Teitelboim, E. M. Chan, N. J. Borys, P. J. Schuck, C. Dames, *Nat. Commun.* **2018**, *9*, 4907.
- [27] J. C. Martins, A. R. N. Bastos, R. A. S. Ferreira, X. Wang, G. Chen, L. D. Carlos, *Adv. Photonics Res.* **2021**, *2*, 2000169.
- [28] R. G. Geitenbeek, H. W. de Wijn, A. Meijerink, *Phys. Rev. Appl.* **2018**, *10*, 064006.
- [29] D. Pugh-Thomas, B. M. Walsh, M. C. Gupta, *Nanotechnology* **2011**, *22*, 185503.
- [30] C. D. S. Brites, E. D. Martínez, R. R. Urbano, C. Rettori, L. D. Carlos, *Front. Chem.* **2019**, *7*, 267.
- [31] A. S. Souza, L. A. O. Nunes, I. G. N. Silva, F. A. M. Oliveira, L. L. da Luz, H. F. Brito, M. C. F. C. Felinto, R. A. S. Ferreira, S. A. Júnior, L. D. Carlos, O. L. Malta, *Nanoscale* **2016**, *8*, 5327.
- [32] S. Balabhadra, M. L. Debasu, C. D. S. Brites, R. A. S. Ferreira, L. D. Carlos, *J. Phys. Chem. C* **2017**, *121*, 13962.
- [33] F. J. Caixeta, A. R. N. Bastos, A. M. P. Botas, L. S. Rosa, V. S. Souza, F. H. Borges, A. N. C. Neto, A. Ferrier, P. Goldner, L. D. Carlos, R. R. Gonçalves, R. A. S. Ferreira, *J. Phys. Chem. C* **2020**, *124*, 19892.
- [34] M. Back, E. Casagrande, C. A. Brondin, E. Ambrosi, D. Cristofori, J. Ueda, S. Tanabe, E. Trave, P. Riello, *ACS Appl. Nano Mater.* **2020**, *3*, 2594.
- [35] E. D. Martínez, C. D. S. Brites, L. D. Carlos, A. F. García-Flores, R. R. Urbano, C. Rettori, *Adv. Funct. Mater.* **2019**, *29*, 1807758.
- [36] A. N. Carneiro Neto, E. Mamontova, A. M. P. Botas, C. D. S. Brites, R. A. S. Ferreira, J. Rouquette, Y. Guari, J. Larionova, J. Long, L. D. Carlos, **2021**, submitted.
- [37] J. F. C. B. Ramalho, S. F. H. Correia, L. Fu, L. M. S. Dias, P. Adão, P. Mateus, R. A. S. Ferreira, P. S. André, *npj Flex. Electron.* **2020**, *4*, 11.
- [38] L. D. Carlos, V. de Zea Bermudez, R. A. S. Ferreira, L. Marques, M. Assunção, *Chem. Mater.* **1999**, *11*, 581.
- [39] F. Miller, S. Wintzheimer, J. Prieschl, V. Strauss, K. Mandel, *Adv. Opt. Mater.* **2021**, *9*, 2001972.
- [40] J. V. Rival, P. Myrmoona, R. Vinoth, A. M. V. Mohan, E. S. Shibu, *ACS Appl. Mater. Interfaces* **2021**, *13*, 10583.
- [41] R. A. S. Ferreira, P. S. André, J. F. C. B. Ramalho, L. D. Carlos, Universidade de Aveiro and Instituto de Telecomunicações, Internacional WO2021001767 **2020**.
- [42] E. Runge, E. K. U. Gross, *Phys. Rev. Lett.* **1984**, *52*, 997.
- [43] A. N. Carneiro Neto, E. E. S. Teotonio, G. F. de Sá, H. F. Brito, J. Legendziewicz, L. D. Carlos, M. C. F. C. Felinto, P. Gawryszewska, R. T. Moura, R. L. Longo, W. M. Faustino, O. L. Malta, in *Handbook on the Physics and Chemistry Rare Earths*, Vol. 56 (Eds.: J.-C. G. Bünzli, V. K. Pecharsky), Elsevier, Amsterdam **2019**, p. 310.
- [44] W. J. C. Grant, *Phys. Rev. B* **1971**, *4*, 648.
- [45] P. S. André, R. A. S. Ferreira, *Electron. Lett.* **2014**, *50*, 1828.
- [46] L. D. Carlos, R. A. S. Ferreira, V. de Zea Bermudez, S. J. L. Ribeiro, *Adv. Funct. Mater.* **2001**, *11*, 111.
- [47] L. D. Carlos, R. A. S. Ferreira, R. N. Pereira, M. Assunção, V. de Zea Bermudez, *J. Phys. Chem. B* **2004**, *108*, 14924.
- [48] S. S. Nobre, P. P. Lima, R. A. S. Ferreira, R. O. Freire, L. Fu, U. Pischel, V. de Zea Bermudez, O. L. Malta, L. D. Carlos, *J. Phys. Chem. C* **2007**, *111*, 3275.
- [49] M. J. Beltrán-Leiva, E. Solis-Céspedes, D. Páez-Hernández, *Dalt. Trans.* **2020**, *49*, 7444.
- [50] M. A. El-Sayed, *J. Chem. Phys.* **1963**, *38*, 2834.
- [51] M. Kasha, *Discuss. Faraday Soc.* **1950**, *9*, 14.
- [52] R. Sen, S. Paul, A. Sarkar, A. M. P. Botas, A. N. Carneiro Neto, P. Brandão, A. M. L. Lopes, R. A. S. Ferreira, J. P. Araújo, Z. Lin, *CrystEngComm* **2021**, *23*, 4143.
- [53] C. D. S. Brites, A. Millán, L. D. Carlos, in *Handbook on the Physics and Chemistry Rare Earths*, Vol. 49 (Eds.: J.-C. G. Bünzli, V. K. Pecharsky), Elsevier, Amsterdam **2016**, p. 281.
- [54] E. V. Salerno, J. Zeler, S. V. Eliseeva, M. A. Hernández-Rodríguez, A. N. Carneiro Neto, S. Petoud, V. L. Pecoraro, L. D. Carlos, *Chem.—A Eur. J.* **2020**, *26*, 13792.
- [55] M. Rodrigues, R. Piñol, G. Antorrena, C. D. S. Brites, N. J. O. Silva, J. L. Murillo, R. Cases, I. Díez, F. Palacio, N. Torras, J. A. Plaza, L. Pérez-García, L. D. Carlos, A. Millán, *Adv. Funct. Mater.* **2016**, *26*, 200.
- [56] C. D. S. Brites, M. C. Fuertes, P. C. Angelomé, E. D. Martínez, P. P. Lima, G. J. A. A. Soler-Illia, L. D. Carlos, *Nano Lett.* **2017**, *17*, 4746.

- [57] K. Nigoghossian, Y. Messaddeq, D. Boudreau, S. J. L. Ribeiro, *ACS Omega* **2017**, 2, 2065.
- [58] A. Skripka, A. Benayas, R. Marin, P. Canton, E. Hemmer, F. Vetrone, *Nanoscale* **2017**, 9, 3079.
- [59] O. A. Savchuk, J. J. Carvajal, C. D. S. Brites, L. D. Carlos, M. Aguilo, F. Diaz, *Nanoscale* **2018**, 10, 6602.
- [60] A. R. N. Bastos, C. D. S. Brites, P. A. Rojas-Gutierrez, C. DeWolf, R. A. S. Ferreira, J. A. Capobianco, L. D. Carlos, *Adv. Funct. Mater.* **2019**, 29, 1905474.
- [61] Y. Chen, J. He, X. Zhang, M. Rong, Z. Xia, J. Wang, Z. Q. Liu, *Inorg. Chem.* **2020**, 59, 1383.
- [62] M. Jia, Z. Sun, H. Xu, X. Jin, Z. Lv, T. Sheng, Z. Fu, *J. Mater. Chem. C* **2020**, 8, 15603.
- [63] O. Savchuk, J. J. Carvajal Marti, C. Cascales, P. Haro-Gonzalez, F. Sanz-Rodríguez, M. Aguilo, F. Diaz, *Nanomaterials* **2020**, 10, 993.
- [64] M. Sójka, C. D. S. Brites, L. D. Carlos, E. Zych, *J. Mater. Chem. C* **2020**, 8, 10086.
- [65] A. Cadiau, C. D. S. Brites, P. M. F. J. Costa, R. A. S. Ferreira, L. D. Carlos, *ACS Nano* **2013**, 7, 7213.
- [66] S. Wang, S. Ma, J. Wu, Z. Ye, X. Cheng, *Chem. Eng. J.* **2020**, 393, 124564.
- [67] Z. Zhang, H. Suo, X. Zhao, C. Guo, *Photonics Res.* **2020**, 8, 32.
- [68] D. Zhao, X. Han, S. Wang, J. Liu, Y. Lu, C. Li, *Chem.—A Eur. J.* **2020**, 26, 3145.
- [69] S. Liang, Y. Wang, X. Wu, M. Chen, L. Mu, G. She, W. Shi, *Chem. Commun.* **2019**, 55, 3509.
- [70] C. Mi, J. Zhou, F. Wang, G. Lin, D. Jin, *Chem. Mater.* **2019**, 31, 9480.
- [71] M. L. Debasu, D. Ananias, I. Pastoriza-Santos, L. M. Liz-Marzán, J. Rocha, L. D. Carlos, *Adv. Mater.* **2013**, 25, 4868.
- [72] T. Wang, P. Li, H. Li, *ACS Appl. Mater. Interfaces* **2014**, 6, 12915.
- [73] S. Zheng, W. Chen, D. Tan, J. Zhou, Q. Guo, W. Jiang, C. Xu, X. Liu, J. Qiu, *Nanoscale* **2014**, 6, 5675.
- [74] Y. Zhou, B. Yan, F. Lei, *Chem. Commun.* **2014**, 50, 15235.
- [75] S. Balabhadra, M. L. Debasu, C. D. S. Brites, L. A. O. Nunes, O. L. Malta, J. Rocha, M. Bettinelli, L. D. Carlos, *Nanoscale* **2015**, 7, 17261.
- [76] R. Piñol, C. D. S. Brites, R. Bustamante, A. Martínez, N. J. O. Silva, J. L. Murillo, R. Cases, J. Carrey, C. Estepa, C. Sosa, F. Palacio, L. D. Carlos, A. Millán, *ACS Nano* **2015**, 9, 3134.
- [77] Y. Cui, B. Li, H. He, W. Zhou, B. Chen, G. Qian, *Acc. Chem. Res.* **2016**, 49, 483.
- [78] F. E. Maturi, C. D. S. Brites, E. C. Ximendes, C. Mills, B. Olsen, D. Jaque, S. J. L. Ribeiro, L. D. Carlos, *Laser Photon. Rev.* **2021**, 2100301.
- [79] E. Fujiwara, P. L. Machado, T. C. D. Oliveira, M. C. P. Soares, T. D. Cabral, C. M. B. Cordeiro, in *2019 SBFot Int. Optics Photonics Conf. (Sbfot. IOPC)*, IEEE, Piscataway, NJ **2019**, pp. 1–5.
- [80] Y. Ma, Y. Dong, S. Liu, P. She, J. Lu, S. Liu, W. Huang, Q. Zhao, *Adv. Opt. Mater.* **2020**, 8, 1901687.
- [81] L. Lu, Z. Jiang, Y. Hu, H. Zhou, G. Liu, Y. Chen, Y. Luo, Z. Chen, *Opt. Express* **2019**, 27, 25420.
- [82] M. S. Brown, B. Ashley, A. Koh, *Front. Bioeng. Biotechnol.* **2018**, 6, 47.
- [83] J. Kuht, A. D. Farmery, *Anaesth. Intensive Care Med.* **2014**, 15, 273.
- [84] J. Kuht, A. D. Farmery, *Anaesth. Intensive Care Med.* **2018**, 19, 507.
- [85] J. Zhou, B. del Rosal, D. Jaque, S. Uchiyama, D. Jin, *Nat. Methods* **2020**, 17, 967.
- [86] M. T. Berry, P. S. May, H. Xu, *J. Phys. Chem.* **1996**, 100, 9216.
- [87] W. M. Faustino, L. A. Nunes, I. A. A. Terra, M. C. F. C. Felinto, H. F. Brito, O. L. Malta, *J. Lumin.* **2013**, 137, 269.
- [88] R. A. S. Ferreira, C. D. S. Brites, C. M. S. Vicente, P. P. Lima, A. R. N. Bastos, P. G. Marques, M. Hiltunen, L. D. Carlos, P. S. André, *Laser Photon. Rev.* **2013**, 7, 1027.
- [89] P. Reineck, A. Francis, A. Orth, D. W. M. Lau, R. D. V. Nixon-Luke, I. Das Rastogi, W. A. W. Razali, N. M. Cordina, L. M. Parker, V. K. A. Sreenivasan, L. J. Brown, B. C. Gibson, *Adv. Opt. Mater.* **2016**, 4, 1549.
- [90] J. Xu, J. Zhou, Y. Chen, P. Yang, J. Lin, *Coord. Chem. Rev.* **2020**, 415, 213328.
- [91] L. R. Melby, N. J. Rose, E. Abramson, J. C. Caris, *J. Am. Chem. Soc.* **1964**, 86, 5117.
- [92] M. Fang, A. G. Bispo Jr, L. Fu, R. A. S. Ferreira, L. D. Carlos, *J. Lumin.* **2020**, 219, 116910.
- [93] J. F. C. B. Ramalho, L. C. F. António, S. F. H. Correia, L. S. Fu, A. S. Pinho, C. D. S. Brites, L. D. Carlos, P. S. André, R. A. S. Ferreira, *Opt. Laser Technol.* **2018**, 101, 304.
- [94] M. J. Frisch, G. W. Trucks, H. B. Schlegel, G. E. Scuseria, M. A. Robb, J. R. Cheeseman, G. Scalmani, V. Barone, B. Mennucci, G. A. Petersson, H. Nakatsuji, M. Caricato, X. Li, H. P. Hratchian, A. F. Izmaylov, J. Bloino, G. Zheng, J. L. Sonnenberg, M. Hada, M. Ehara, K. Toyota, R. Fukuda, J. Hasegawa, M. Ishida, T. Nakajima, Y. Honda, O. Kitao, H. Nakai, T. Vreven, J. J. A. Montgomery, et al., *Gaussian 09, Revision D.01*, Gaussian, Inc., Wallingford, CT **2016**.
- [95] A. D. Becke, *J. Chem. Phys.* **1993**, 98, 5648.
- [96] C. Lee, W. Yang, R. G. Parr, *Phys. Rev. B* **1988**, 37, 785.
- [97] M. Dolg, H. Stoll, H. Preuss, *J. Chem. Phys.* **1989**, 90, 1730.
- [98] O. L. Malta, *Chem. Phys. Lett.* **1982**, 87, 27.
- [99] R. T. Moura, A. N. Carneiro Neto, R. L. Longo, O. L. Malta, *J. Lumin.* **2016**, 170, 420.
- [100] A. N. Carneiro Neto, R. T. Moura, E. C. Aguiar, C. V. Santos, M. A. F. L. B. de Medeiros, *J. Lumin.* **2018**, 201, 451.
- [101] R. T. Moura Jr., A. N. Carneiro Neto, E. C. Aguiar, C. V. Santos Jr., E. M. de Lima, W. M. Faustino, E. E. S. Teotonio, H. F. Brito, M. C. F. C. Felinto, R. A. S. Ferreira, L. D. Carlos, R. L. Longo, O. L. Malta, *Opt. Mater. X* **2021**, 11, 100080.
- [102] E. Kasprzycka, A. N. Carneiro Neto, V. A. Trush, L. Jerzykiewicz, V. M. Amirkhanov, O. L. Malta, J. Legendziewicz, P. Gawryszewska, *J. Rare Earths* **2020**, 38, 552.
- [103] R. T. Moura, J. A. Oliveira, I. A. Santos, E. M. Lima, L. D. Carlos, E. C. Aguiar, A. N. C. Neto, *Adv. Theory Simulations* **2021**, 4, 2000304.
- [104] P. P. Lima, S. S. Nobre, R. O. Freire, S. A. Júnior, R. A. S. Ferreira, U. Pischel, O. L. Malta, L. D. Carlos, *J. Phys. Chem. C* **2007**, 111, 17627.
- [105] T. Yamase, in *Handbook on the Physics and Chemistry Rare Earths*, (Eds.: J. Karl, A. Gschneidner, J.-C. G. Bünzli, V. K. Pecharsky), Elsevier, Amsterdam, **2009**, pp. 297–356.
- [106] Y. H. Pham, V. A. Trush, A. N. Carneiro Neto, M. Korabik, J. Sokolnicki, M. Weselski, O. L. Malta, V. M. Amirkhanov, P. Gawryszewska, *J. Mater. Chem. C* **2020**, 8, 9993.
- [107] E. Kasprzycka, V. A. Trush, V. M. Amirkhanov, L. Jerzykiewicz, O. L. Malta, J. Legendziewicz, P. Gawryszewska, *Chem.—A Eur. J.* **2017**, 23, 1318.
- [108] L. Fu, R. A. S. Ferreira, M. Fernandes, S. C. Nunes, V. de Zea Bermudez, G. Hungerford, J. Rocha, L. D. Carlos, *Opt. Mater. (Amst)*. **2008**, 30, 1058.
- [109] T. Miyakawa, D. L. Dexter, *Phys. Rev. B* **1970**, 1, 2961.
- [110] E. Hairer, G. Wanner, in *Encyclopedia of Applied and Computational Mathematics* (Ed.: B. Engquist), Springer Berlin Heidelberg, Berlin, Heidelberg **2015**, pp. 1213–1216.